

Chapter 4

The Oxygen Derived Database and Its Application to the Solar Atmosphere

In observational studies of characteristics of the solar chromosphere and transition region, planned for the SOHO spacecraft, spectral emission by ions of oxygen will be of major importance. Determination of the coronal peak temperature, studies of differential emission measure, abundance separation, sunspot velocity fields and other dynamic flows, are all dependent, to some degree, on spectral measurements of oxygen ion emission line intensities (Harrison & Fludra(1995), Wilhelm (1993)). In previous studies, interpretation of data has often been confused by uncertainties in the accuracy of the atomic collision database underpinning the spectral reduction and in the appropriateness of simplifying assumptions in excited ion population and ionisation state models. Here, a critical review is given of the completeness and precision of the fundamental atomic collision data entering prediction of emission. This is based on the recommendations of Lang et al.(1994). Analysis of the reproduction of atomic data, from fitting procedures presented in the general literature, is also undertaken. A detailed examination of derived atomic data is presented which includes analysis of the influence of metastable states and finite plasma electron density. The importance

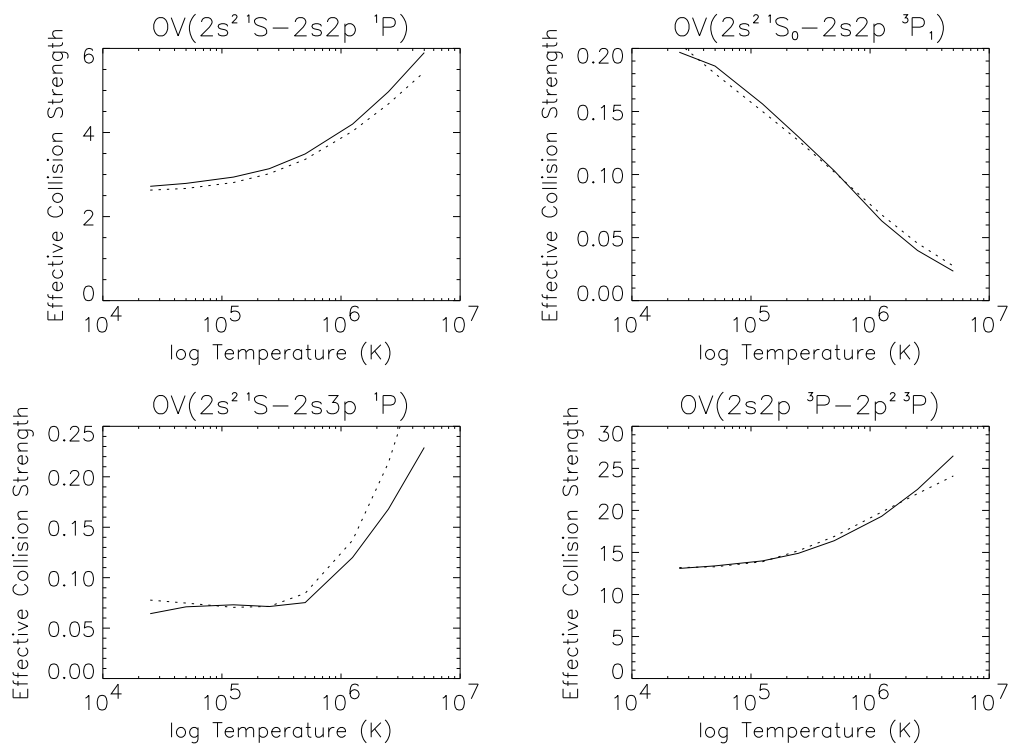


Figure 4.1: Comparison of the effective collision strength data from Kato et al.(1990) and the ADAS database for potential diagnostic transitions. The data of Kato et al.(1990) is the solid line and the older ADAS data (see text for details) is the dotted line.

of this type of approach was outlined in chap. 2. In fact, it is stressed that a complete description of light ion emission from plasmas must include these effects and that this is only possible through the adoption of a generalised collisional-radiative model. A paper is in preparation (Brooks et al.(1997)) which makes comparative analysis with existing derived atomic data, used in spectral analysis, and includes the effects of dynamic ionisation. Re-examination from this viewpoint allows us to quantify systematic errors introduced to the analysis by common simplifications and assumptions.

For practical application, and especially for the spectrometers on board the SOHO

satellite, certain contribution functions, diagnostic line intensity ratios, photon efficiencies etc. are of special importance and general interest in the astrophysical community. Scientific interest will focus around diagnostic spectral analysis of ions formed in the high temperature/low density transition zone. OII has been identified as occurring in this region but ions such as OIII, OIV, OV and OVI have greater prevalence and consequently greater diagnostic impact. Accuracy in the interpretation of SOHO data and in probing the key physical mechanisms present in the solar atmosphere can only be maintained through detailed quantitative modelling of the relevant atomic physics. A comprehensive basis of derived atomic data for analysis of oxygen ion emission and for modelling oxygen ion population distributions has been prepared, and is continually being updated, which spans both these and also laboratory fusion needs. Confidence in the results of our atomic modelling is based on its ability to account correctly for the influence of density, and excited state lifetime variations, between the different plasma regimes to which it is applied. The derived data are archived within ADAS. The oxygen data represents the most complete availability at the present time and provides a prescription for modelling the radiating characteristics of atoms and ions in solar plasmas using ADAS.

4.1 Upgrade of Oxygen Fundamental Database

We seek the best possible derived emissivity data to support the objectives of the SOHO mission. To this end it has been necessary to review and upgrade the fundamental electron impact collision cross-section data which enters our derived calculations. This is a rapidly changing situation.

4.1.1 Quality and Accuracy of Electron Impact Excitation Data - Comparison to Previous Work

Using the publication of Lang et al.(1994) as a benchmark, we have updated the existing ADAS database for oxygen ions. In addition, more recent calculations, presented in the general literature, have been incorporated where appropriate.

Transition	Comments on accuracy
$OV(2p^2\ ^3P - 2s^2\ ^1S)$	27.6% more at $2.5 \times 10^4 K$ reducing to 2% at $5 \times 10^4 K$ then increasing to 143% at $5 \times 10^6 K$.
$OV(2p^2\ ^1S - 2s^2\ ^1S)$	48.3% more at $2.5 \times 10^4 K$ increasing to a max. at $2.5 \times 10^5 K$ of 87.8% then reducing eventually to 20.8% less at $5 \times 10^6 K$.
$OV(2p^2\ ^1S - 2s2p\ ^3P)$	27.3% more at $2.5 \times 10^4 K$ increasing to a max. at $2.5 \times 10^5 K$ of 106.0% then reducing to 61.4% at $5 \times 10^6 K$.
$OV(2s3s\ ^3S - 2s2p\ ^3P)$	60% more at $2.5 \times 10^4 K$ reducing to 1% at $1.25 \times 10^6 K$ then increasing to 100% at $5 \times 10^6 K$.
$OV(2s3s\ ^1S - 2s2p\ ^3P)$	58% more at $2.5 \times 10^4 K$ reducing to 2% at $5 \times 10^5 K$. Dips then increases to 56% at $5 \times 10^6 K$.
$OV(2s3p\ ^1P - 2s2p\ ^3P)$	57% more at $2.5 \times 10^4 K$ reducing to 3% at $5 \times 10^5 K$. Increasing to 32% at $5 \times 10^6 K$.
$OV(2p^2\ ^3P_2 - 2p^2\ ^3P_0)$	51% less at $2.5 \times 10^4 K$ reducing to 25% at $5 \times 10^5 K$ then increasing to 52% at $5 \times 10^6 K$.
$OV(2p^2\ ^3P_2 - 2p^2\ ^3P_1)$	73% less at $2.5 \times 10^4 K$ reducing to 35% at $5 \times 10^5 K$ then increasing to 60% at $5 \times 10^6 K$.
$OV(2p^2\ ^1S - 2s2p\ ^3P)$	Increases to 46.9% at $5 \times 10^5 K$ then reduces to 29% at $5 \times 10^6 K$.

Table 4.1: Comments on the accuracy of the effective collision strength data of Kato et al.(1990) as compared to the ADAS database for lines which show deviations of greater than 20%.

Berrington (1994) reviewed and assessed the current state of the fundamental atomic collision data for beryllium like ions. This included OV and he recommended the results of Kato, Lang, & Berrington (1990). These authors published parameters of an analytic fit to effective collision strengths among the $n = 2$ and $n = 3$ levels, including fine structure transitions. These were obtained from an **R**-matrix calculation involving the 26 lowest lying states (Berrington & Kingston -unpublished). We followed the prescribed method for calculating the effective collision strengths suggested by Kato et al., and then made a detailed comparison of the results with the OV data archived within ADAS. The older data consisted of results from the **R**-matrix calculations of Berrington et al.(1979), Berrington et al.(1985), Widing et al.(1982) and Tayal et al.(1982) and was supplemented by Born calculations (Summers (1992)-unpublished). The results of the comparison for four of the most important transitions of diagnostic interest to CDS and/or SUMER are displayed in fig.4.1. The solid line is the newer data of Kato et al. while the dotted line is the older data. The OV resonance line ($2s^2\ ^1S - 2s2p\ ^1P$) is within 8% of the older data at all temperatures. The intersystem fine structure transition $OV(2s^2\ ^1S_0 - 2s2p\ ^3P_1)$ is within 7%, of the older data, until $\sim 2.5 \times 10^6 K$ where the disparity begins to increase, eventually rising to 17.5% at $\sim 5 \times 10^6 K$. The $OV(2s^2\ ^1S - 2s3p\ ^1P)$ shows this same behaviour except that it has a greater overall deviation, i.e. $\sim 20\%$ until the gap begins to increase, at the same temperature, rising to $\sim 41\%$. The $OV(2s2p\ ^3P - 2p^2\ ^3P)$ transition data is within 3% all the way up to $\sim 5 \times 10^6 K$ where it diverges by up to $\sim 9\%$. Comments on the transitions which showed the greatest deviations from the older data are given in table 4.1. The effective collision strengths for all the other transitions were found to agree with the older data to within 20%, except at high temperatures, and in many cases far better than 15%. We should note that the deviations at the highest temperatures ($\sim 5 \times 10^5 K$) were principally due to the nature of the ADAS extrapolation routine used on the older data. This automatically flattened off the effective collision strengths at high temperature when no data was available for a particular transition. In fact, this may also explain why smaller upturns were often found (see fig.4.1). Discrepancies at low temperatures were generally not seen, but in one case, the $2s2p\ ^3P$ to $2s3p\ ^3P$ transition, there was a deviation of $\sim 40\%$.

The largest deviation, from the older data, we discovered was in the $OV(2s2p^3P - 2s3s^3S)$ transition. This was due to an error in the fit parameters of Kato et al.(1990). The discrepancy was considerably reduced after amendment Kato(1994). We also found that the fit parameters supplied for transitions between the fine structure levels of the $2p^2^3P$ term produced effective collision strengths that compared well with the older data, but that the excitation rate coefficients derived from them, using the formula suggested by Kato et al., did not correspond to the published graphs. Kato(1994) confirmed that this was a publishing mistake. Following these private communications it was decided to obtain the original Belfast calculations and compare every effective collision strength with those calculated using the published fit parameters. As a result, other publishing mistakes were identified involving the following transitions.

$$\begin{aligned}
 &2s3p^3P_2 - 2s3p^3P_2 \\
 &2s3s^1S - 2s2p^1P \\
 &2s3s^3S - 2s^2^1S \\
 &2s3d^1D - 2s3s^1S
 \end{aligned}$$

In addition, it was found that a number of fine structure transitions were reproduced to worse than 10% by the approximate fit method of Kato et al. These have been noted in the adf04 file and are within 25% with the exception of the $2p^2^3P_2$ to $2p^2^3P_0$ and 3P_1 transitions which are $\sim 38\%$ and $\sim 53\%$ respectively.

In the case of nitrogen like ions, Kato (1994) was the reviewer and assessor and she made recommendations as to which sources should be used for certain transitions amongst the excited states of OII. However, since the review McLaughlin & Bell (1994) have completed a calculation of effective collision strengths in LS coupling for OII using an **R**-matrix approximation which takes account of the eleven lowest lying states of the ion. They provide a table of the coefficients of a chebyshev polynomial approximation to their calculated effective collision strengths. The fit accuracy is stated to be better than 1% for most transitions, and better than 2% at worst.

ADAS contains an adf04 file consisting of close-coupling data from Ho & Henry (1983), Pradhan (1976) and Born approximation calculations of Summers (1992). We

Transition	ADAS data source	Comments on associated spectral line
OII($2p^3\ ^2D - 2p^2(^3P)3s\ ^2P$)	Summers	CS
OII($2p^3\ ^2P - 2s2p^4\ ^2S$)	no previous data	CS
OII($2p^3\ ^2D - 2s2p^4\ ^2D$)	no previous data	CS
OII($2p^3\ ^4S - 2s2p^4\ ^4P$)	Ho & Henry	S
OII($2p^3\ ^4S - 2p^3\ ^2D$)	Pradhan	diagnostic
OII($2p^3\ ^4S - 2p^3\ ^2P$)	Pradhan	diagnostic
OII($2p^3\ ^2D - 2p^3\ ^2P$)	Pradhan	diagnostic

Table 4.2: Selected transitions of interest in OII. The data source are those prior to the work of McLaughlin & Bell (1994). CS denotes that the line is within the CDS & SUMER spectrometer wavelength ranges. The ratios of the three lines marked ‘diagnostic’ are sensitive to electron density and temperature and are useful for studies of planetary nebulae (Kingsburgh & English (1992)).

have updated this file to include the results of McLaughlin & Bell, adding new data and replacing older data that has been superseded. However, we have retained data for transitions that were not calculated by McLaughlin & Bell. A comparison was also made between transitions for which old and new data were available.

Four transitions between excited terms of OII give rise to spectral lines within the observable range of either the CDS or SUMER instrument (see table.4.2, which also shows potential diagnostic transitions for planetary nebulae). No values prior to those of McLaughlin & Bell were available for the OII($2p^3\ ^2P - 2s2p^4\ ^2S$) and OII($2p^3\ ^2D - 2s2p^4\ ^2D$) transitions. A comparison between the results of Ho & Henry (1983) for the OII($2p^3\ ^4S - 2s2p^4\ ^4P$) transition and Pradhan (1976) for the OII($2p^3\ ^4S - 2p^3\ ^2D$), OII($2p^3\ ^4S - 2p^3\ ^2P$) and OII($2p^3\ ^2D - 2p^3\ ^2P$) transitions, with the results of McLaughlin & Bell (1994) has already been discussed by McLaughlin & Bell (1993); however, fig.4.2 shows these deviations. It can be seen that the Ho & Henry results are within 18% at all temperatures, although they slightly overestimate below 2×10^5 K and then underestimate above this threshold. Pradhan’s data, for the two transitions to the ground state, are generally diverging from that of McLaughlin & Bell until $\sim 4 \times 10^5$ K. This divergence is never more than $\sim 20\%$ below $\sim 8 \times 10^4$ K

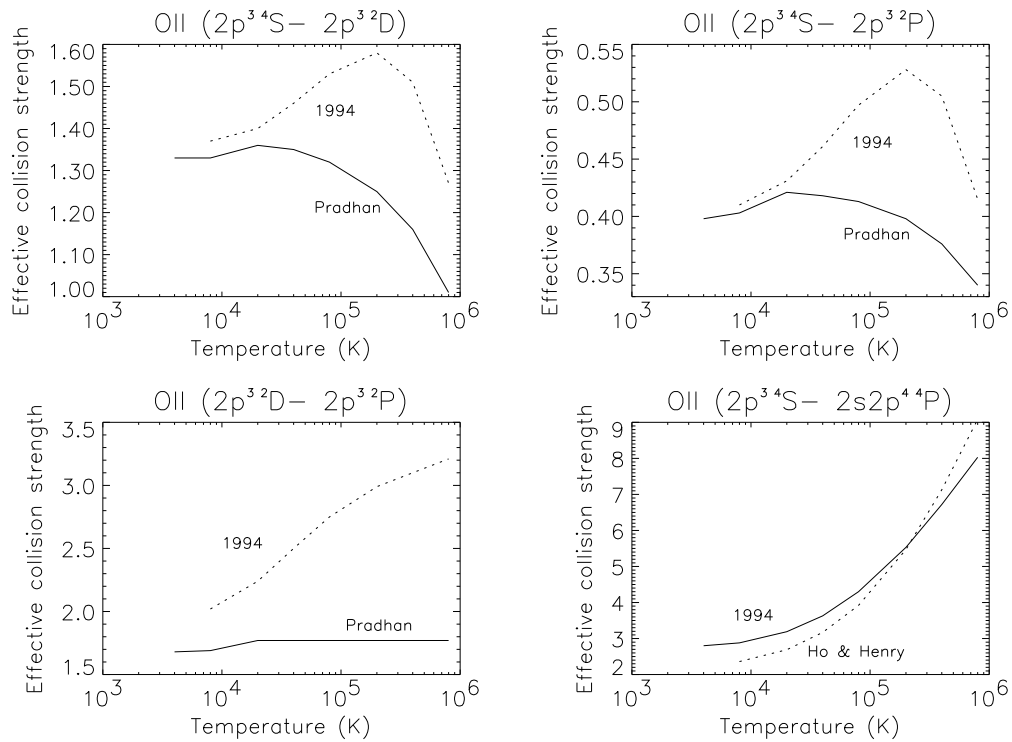


Figure 4.2: Comparison of the effective collision strength data of Ho & Henry (1983), Pradhan(1976) and McLaughlin & Bell (1994), for selected transitions. 1994 refers to the data of McLaughlin & Bell.

and takes its' peak value of 34% at $4 \times 10^5 K$, for the $^2P - ^4S$ transition. The new data for the $^2P - ^2D$ transition appears to be significantly larger than that of Pradhan. It is already 19.5% larger at $8 \times 10^3 K$ and the disparity continues to grow until the newer data is $\sim 81\%$ greater at the highest temperatures.

For the $OII(2p^3 \ ^2D - 2p^2(^3P)3s \ ^2P)$ transition we found that the Born approximation calculations of Summers were surprisingly close to the higher quality calculations of McLaughlin & Bell. At low temperatures ($\sim 8 \times 10^3 K$) the results of Summers overestimate by about 30%, thereafter, the results converge until those of McLaughlin & Bell become larger at $\sim 1 \times 10^4 K$. The two calculations subsequently diverge until

those of Summers underestimate by about 57% at $\sim 8 \times 10^5 K$. The only other transitions for which a comparison could be made were the $OII(2p^3 \ ^2P - 2p^2(^3P)3s \ ^2P)$ and $OII(2p^3 \ ^4S - 2p^2(^3P)3s \ ^4P)$ transitions. In the older dataset, the former transition was again Born approximation data from Summers, and the latter transition originated from Ho & Henry (1983). Once again the Born approximation data proved to be reasonably accurate. This time within ~ 51 - 61% at all temperatures. For the other transition, the results of Ho & Henry were within $\sim 16\%$ above $\sim 2 \times 10^4 K$. Initially they underestimated but above $\sim 2.5 \times 10^4 K$ they always overestimated.

New transition probabilities have also been calculated, for some transitions, using the length values for the relativistic oscillator strengths given in Table.VI of Bell, Hibbert, Stafford & McLaughlin (1994). If no new data was available, the older data (Luken & Sinanoglu (1976), Weise, Smith & Glennon (1966) and Summers (1992)) was retained.

The current state of the ADAS atomic collision database, for the rest of the ions along the oxygen isonuclear sequence, is summarised in tables.4.3 and 4.4.

Recently Aggarwal (1993) published new effective collision strengths for transitions amongst 26 LS-coupled states of the following configurations,

$$\begin{aligned} &(1s^2)2s^22p^2, \quad (1s^2)2s2p^3 \\ &\quad (1s^2)2p^4, \quad (1s^2)2s^22p3s \\ &(1s^2)2s^22p3p, \quad (1s^2)2s^22p3d \end{aligned}$$

with transitions amongst the latter three being reported for the first time. Aggarwal used the R-matrix method with total angular momentum $L \leq 12$ for forbidden transitions with an extension to higher partial waves, $12 \leq L \leq 40$, for optically allowed and semi-forbidden (spin allowed, parity forbidden) transitions by means of the no-exchange R-matrix code of Burke, Burke & Scott (1992). Contributions from resonances were also included. Aggarwal estimates these new results to be accurate to 10% for transitions amongst the lower excited states and about 20% for those amongst the higher excited states. Aggarwal also states that agreement with his previous calculations (see table) is generally better than 25%. He finds some differences for individual transitions due to the inclusion of resonances and proposes to assess

Ion & Reviewer	Recommendations	ADAS data sources
OI- Lang & Summers	Experimentally determined cross-sections recommended by Laher & Gilmore(1990), between the $2s^2 2p^4 \ ^3P$ ground and $2s^2 2p^4 \ ^1D, \ ^1S, 2s^2 2p^3 3s \ ^5S, \ ^3S, 2s^2 2p^3 \ ^5P, \ ^3P$ and $2s^2 2p^3 3d \ ^5D, \ ^3D$	As recommended. Supplemented with data from Summers(1992).
OIII- Monsignori-Fossi & Landini	R-matrix results for optically allowed transitions (Aggarwal(1985)), and forbidden transitions (Aggarwal(1983)) between $2s^2 2p^2, 2s 2p^3$ and $2p^4$. Distorted wave calculations of Bhatia et al.(1979) for transitions not covered in above two papers.*	As recommended, supplemented with data from Summers(1992) for transitions involving levels of $2s^2 2p(^2P)3l$
OIV- Sampson, Zhang & Fontes	Close coupling R-matrix results of Blum & Pradhan(1992) for fine structure transitions between levels of the $2s^2 2p, 2s 2p^2$ & $2p^3$ terms, except the 1-2 transition, where the calculations of Hayes & Nussbaumer (1983) are preferred. They also suggest a supplemental calculation to higher energies.**	Contains close-coupling calculations of Hayes (1983) from $2s^2 2p \ ^2P$ & $2s 2p^2 \ ^4P$ to the 8 lowest lying levels Robb (1980) for transitions between $2s 2p^2 \ ^2S, \ ^2P$ & $\ ^2D$. Supplemented with Summers data for n=2-2, 3-3, & others involving n=2.

Table 4.3: Current state of the ADAS atomic data library for the low charge oxygen ions not discussed in the text. For more details see Summers(1996), Lang & Summers (1995)-ADAS document. *See text. **Zhang(1994) has now completed this calculation and the results are due for inclusion.

Ion & Reviewer	Recommendations	ADAS data sources
OVI-McWhirter	Relativistic distorted wave calculations of Zhang et al.(1990) altered to include resonance effects (for 2s-3s,3p & 2p-3s,3p) and to converge with close-coupling results (for 2s-3p, 2p-3s,3p,3d), following the work of Bhadra & Henry(1982).	As recommended. Supplemented with data from Summers(1992).
OVII-Dubau	Data from the review by Kato & Nakazaki(1989) for $1s^2 - 1s2l$, Zhang & Sampson (1987) for transitions within $1s2l$, Tayal & Kingston(1984) & Sampson, Goett & Clark(1983) for $1s^2 - 1snl$ n=3 and above.	As recommended except amongst $1s2l$ where the results of Pradhan et al.(1981) were used.*
OVIII-Callaway	Close coupling results of Abu-Salbi & Callaway(1981) for 1s-n=2 transitions.	Born Approximation data of Summers (1992)

Table 4.4: Current state of the ADAS atomic data library for the moderately high charge oxygen ions not discussed in the text. For more details see Summers(1996), Lang & Summers (1995)-ADAS document. *-Under review.

$\lambda 1302\text{\AA}$, $\lambda 1305\text{\AA}$, $\lambda 1306\text{\AA}$	SUMER: detailed study of fine loop structures in the corona.
$\lambda 1152.1\text{\AA}$, $\lambda 1355.59\text{\AA}$, $\lambda 1358.5\text{\AA}$	Within SUMER range 1st order.

Table 4.5: OI emission lines and their application to SOHO-CDS and/or SUMER

their accuracy in due course. These results have been incorporated into an updated adf04 file and will be included in the central ADAS database after the inclusion of radiative recombination data has been completed. Lennon & Burke(1994) also published Maxwellian- averaged collision strengths. However, Dere et al.(1996) found no appreciable differences from the results of Aggarwal(1983).

4.2 The use of Oxygen Data for SOHO-CDS and SOHO-SUMER Spectroscopy

Brief descriptions and associated references for more information on CDS & SUMER were given in chap.1. Based upon their spectral wavelength coverage and sensitivities, sets of observable spectrum lines have been identified which have diagnostic impact on the solar atmospheric structure. These spectrum lines are forming the basis of coordinated observing sequences. Using the Blue Book and the Red Book (Wilhelm et al.(1993)), we have identified important emission lines of oxygen ions that have been selected for observing sequences. Tables 4.5 to 4.11 summarise these lines and their applications.

The majority of lines mentioned in tables 4.9 and 4.10 are expected also to be used in a CDS campaign to check on the atomic physics of the OV ion.

In practice, sub-selections of the above lines are made to form observing sequences with specific diagnostic purposes such as identification of high velocity events or differential emission measure analysis of the quiet sun. It is convenient in the preparation

$\lambda 833.34\text{\AA}$	Within SUMER range 1st order.
$\lambda 644.1\text{\AA}$	Within SUMER range 2nd order.
$\lambda 616.6\text{\AA}$	Within CDS range and SUMER range 2nd order.
$\lambda 718.5\text{\AA}$	Within CDS range and SUMER range 2nd order.

Table 4.6: OII emission lines and their application to SOHO-CDS and/or SUMER

$\lambda 702.9\text{\AA}$, $\lambda 525.8\text{\AA}$	Within CDS range and SUMER range 2nd order.
$\lambda 703.9\text{\AA}$	CDS: Study of He enhancement in the transition zone, study of line broadening as an indicator of MHD waves
$\lambda 599.6\text{\AA}$ $\lambda 1015.36\text{\AA}$	High velocity events. SUMER: relationship between high/low density structures in the solar atmosphere.
$\lambda 507.6\text{\AA}$	Within SUMER range 2nd order.
$\lambda 718.5\text{\AA}$	Within CDS range and SUMER range 2nd order.
$\lambda 834.46\text{\AA}$	Within SUMER range.

Table 4.7: OIII emission lines and their application to SOHO-CDS and/or SUMER. Note that the OIII($\lambda 599.6\text{\AA}/\lambda 703.9\text{\AA}$) line ratio is a CDS temperature diagnostic.

$\lambda 790.2\text{\AA}$	CDS: dynamic analysis.
$\lambda 553.34\text{\AA}$, $\lambda 554.08\text{\AA}$, $\lambda 555.28\text{\AA}$, $\lambda 608.40\text{\AA}$, $\lambda 609.8\text{\AA}$	CDS: differential emission measure study of quiet sun.
$\lambda 554.5\text{\AA}$	CDS: solar mass ejection studies, evolution of large scale structures, velocity fields near sunspots, high velocity events, granulation in coronal holes.
$\lambda 1249.28\text{\AA}$	SUMER: relationship of coronal & transition region emission line profiles.
$\lambda 787.7\text{\AA}$	Within SUMER range 2nd order.
$\lambda 1407.39\text{\AA}$	Within SUMER range 1st order.

Table 4.8: OIV emission lines and their application to SOHO-CDS and/or SUMER. Note that the OIV($\lambda 625\text{\AA}/\lambda 790.2\text{\AA}$) line ratio is a CDS density diagnostic and that the OIV($\lambda 1407\text{\AA}/\lambda 1404\text{\AA}$) & OIV($\lambda 790\text{\AA}/\lambda 554\text{\AA}$) ratios are density and temperature diagnostics for SUMER, respectively. The OIV($\lambda 1397.2\text{\AA}$, $\lambda 1399.77\text{\AA}$, $\lambda 1407.39\text{\AA}$, $\lambda 1401.16\text{\AA}$) SUMER lines with the OIV($\lambda 555.28\text{\AA}$) CDS line supporting, produce density sensitive ratios. Finally, the OIV/SIV($\lambda 1404.8\text{\AA}$) ratio is also density sensitive.

$\lambda 629.73\text{\AA}$	CDS: differential emission measure study, dynamics, coronal temperature, high velocity events, flows in the vicinity of prominences, also supports SUMER study of line profiles in transition zone & corona. SUMER: line broadening as a signature of hydromagnetic waves.
$\lambda 172.17\text{\AA}$ $\lambda 758.68\text{\AA}$, $\lambda 760.45\text{\AA}$, $\lambda 761.13\text{\AA}$, $\lambda 762.0\text{\AA}$	CDS: coronal temperature study. CDS: differential emission measure study.
$\lambda 760\text{\AA}$	SUMER/CDS: He enhancement in transition zone.
$\lambda 1218.34\text{\AA}$	SUMER: dynamics, oscillations of sunspots.
$\lambda 1259.46\text{\AA}$	SUMER: study of line profiles in transition zone and corona.
$\lambda 1371.3\text{\AA}$	Within SUMER range 1st order.
$\lambda 672.6\text{\AA}$, $\lambda 675.7\text{\AA}$	Within SUMER range 2nd order.

Table 4.9: OV emission lines and their application to SOHO-CDS and/or SUMER.

$\lambda 760\text{\AA}/\lambda 629.73\text{\AA}^*$	SUMER prime candidate for density diagnostics.
$\lambda 1218\text{\AA}/\lambda 629.73\text{\AA}$	Density diagnostic.
$\lambda 192.9\text{\AA}/\lambda 248.46\text{\AA}$	Density diagnostic.
$\lambda 215.25\text{\AA}/\lambda 220.35\text{\AA}$	Density/temperature diagnostic.
$\lambda 172\text{\AA}/\lambda 630\text{\AA}$	CDS prime candidate for temperature diagnostics.
$\lambda 760\text{\AA}/\lambda 630\text{\AA}$	SUMER prime candidate for density diagnostics.
$\lambda 193\text{\AA}/\lambda 760\text{\AA}$	Temperature diagnostic.
$\lambda 215\text{\AA}/\lambda 193\text{\AA}$	Density/temperature diagnostic.
$\lambda 193\text{\AA}/\lambda 172\text{\AA}$	Density diagnostic.
$\lambda 220\text{\AA}/\lambda 248\text{\AA}$	Temperature diagnostic, also slightly density sensitive.
$\lambda 220\text{\AA}/\lambda 172\text{\AA}$	Slightly density/temperature sensitive.
$\lambda 270.98\text{\AA}/\lambda 215\text{\AA}$	Density diagnostic.
$\lambda 271\text{\AA}/\lambda 215\text{\AA}$	Density diagnostic.
$\text{CaIV}/\text{OV}(\lambda 669.6)\text{\AA}$	Within CDS range.

Table 4.10: OV emission line ratios which are potential diagnostics of temperature and density and are within CDS and/or SUMER wavelength ranges. Wavelengths with places after the decimal point are LSJ resolved the others are summed multiplets. * denotes that fine structure transitions of the OV($\lambda 760\text{\AA}$) line, which are quantum mechanically allowed, also produce density sensitive line ratios.

$\lambda 183.9\text{\AA}$	Within CDS range.
$\lambda 172.93\text{\AA}$	CDS: study of temperature gradient in a coronal hole.
$\lambda 173.1\text{\AA}, \lambda 184.1\text{\AA}$	CDS: study of peak temperature of the corona.
$\lambda 1031.9\text{\AA}$	SUMER: dynamic events, supports CDS peak temperature of corona study, detailed analysis of fine loop structures, flows near prominences, temperature gradient in coronal holes, full sun disc image.
$\lambda 1037.6\text{\AA}$	SUMER: dynamic events, peak temperature of corona, flows near prominences, temperature gradient in coronal holes, full sun disc image.

Table 4.11: OVI emission lines and their application to SOHO-CDS and/or SUMER. Note that the SUMER observed OVI($\lambda 1031.9\text{\AA}, \lambda 1037.6\text{\AA}$) to the CDS observed OVI($\lambda 172.93\text{\AA}, \lambda 173.1\text{\AA}$) ratios are temperature sensitive.

of the theoretical emissivity coefficients, effective contribution functions etc. associated with these measurements, to form a similar grouping called a ‘script’. The script steers the theoretical calculations which prepare these data allowing choice of ionisation balance, contributions to a line from various metastables, recombination etc. A detailed discussion of the specification format is given in sec.3.2.1 and an example (fig. 3.21) is also shown. The script draws from photon emissivity collections stored in ADAS data files of format adf15. In practice, parallel scripts for other elements are also prepared to complete the targeted study. For this work, in which we are primarily concerned with the precision of the atomic basis of analysis, we have prepared a general script that takes account of all the considerations outlined in tables 4.5 to 4.11.

4.3 Collisional-Radiative Modelling

4.3.1 Metastable Resolved Equilibrium Ionisation Balance and Effective Radiated Power

As mentioned in section.2.2.3, it has been usual in describing the ionisation state of ions of oxygen, to assume that the population density is distributed amongst the lowest (ground) levels of each ionisation stage only. Many calculations are available which adequately describe the spectral emission from oxygen ions in many circumstances. Despite this discrepancies do still exist so it is desirable to attempt to explain these by adopting a more complete approach. In accordance with the discussion in chapter.3 sec.3.2.1 we note that the ions of oxygen do have metastable states whose influence should be investigated. For example, the $O^{+4}(2s^2\ ^1S)$ ground and the $O^{+4}(2s2p\ ^3P)$ metastable terms have a population ratio ~ 1.0 in equilibrium at $T_e = 8.1 \times 10^5 K$ and $N_e = 1 \times 10^{10} cm^{-3}$. The high population of a metastable such as $O^{+4}(2s2p\ ^3P)$ is due to its slow collisional relaxation time compared with a normal freely cascading excited population such as that of $O^{+4}(2s3p\ ^1P)$. The result of allowing for this second metastable explicitly is to improve the accuracy of the ionisation balance calculation. This is because, for example, the marked difference in

z	m_z	σ			
		1	2	3	4
0	4	$2s^2 2p^4 \ ^3P$	$2s^2 2p^4 \ ^1D$	$2s^2 2p^4 \ ^1S$	$2s^2 2p^3 3s \ ^5S$
1	3	$2s^2 2p^3 \ ^4S$	$2s^2 2p^3 \ ^2D$	$2s^2 2p^3 \ ^2P$	
2	4	$2s^2 2p^2 \ ^3P$	$2s^2 2p^2 \ ^1D$	$2s^2 2p^2 \ ^1S$	$2s 2p^3 \ ^5S$
3	2	$2s^2 2p \ ^2P$	$2s 2p^2 \ ^4P$		
4	2	$2s^2 \ ^1S$	$2s 2p \ ^3P$		
5	1	$2s \ ^2S$	*		
6	2	$1s^2 \ ^1S$	$1s 2s \ ^3S$		
7	1	$1s \ ^2S$			
8	1	$\ ^1S$			

Table 4.12: Metastable partition of oxygen in LS-coupling. z is the ion charge, m_z is the number of metastables for the z times ionised stage and σ is the metastable index. *At very high densities when $2s \ ^2S$ and $2p \ ^2P$ become closely coupled collisionally, it is useful, in some contexts, to treat $2p$ as a metastable.

dielectronic capture by $O^{+4}(2s^2 \ ^1S)$ and $O^{+4}(2s 2p \ ^3P)$ can be included (see below). As pointed out in chapter.3 sec.3.2.1 and chapter.2 sec.2.1.2, if the timescale of (diffusive) transport across a temperature gradient is of the same order as the collisional timescale then this metastable resolved picture is mandatory. The metastables of O^{+1} and O^{+2} are typically in this situation in the edge of a tokamak. For this work, we solve the metastable resolved equilibrium ionisation balance matrix equation for oxygen as given in eq.3.21. The ground state is also a ‘metastable’ in this notation.

For oxygen, the metastable ‘partition’ is given in table 4.12. The effective coefficients, linking the metastable populations, are also as described in chapter.3 sec.3.2.1. For example, $S_{2s^2 2p \ ^2P \rightarrow 2s 2p \ ^3P}^{3 \rightarrow 4}$ is the coefficient linking the $O^{+3}(2s^2 2p \ ^2P)$ ground state to the $O^{+4}(2s 2p \ ^3P)$ metastable, and in the case of O^{+4} , there is a collisional-radiative coefficient $X_{2s^2 \ ^1S \rightarrow 2s 2p \ ^3P}^{4 \rightarrow 4}$ coupling the two metastable terms.

For a plasma of fixed electron density, N_e , and electron temperature, T_e , with no influx or efflux of oxygen ions, the equilibrium ionisation balance fractional abundances are,

$$\left. \frac{N^z}{N_{tot}} \right|_{equil} \equiv \frac{N^z(t \rightarrow \infty)}{N_{tot}} \quad (4.1)$$

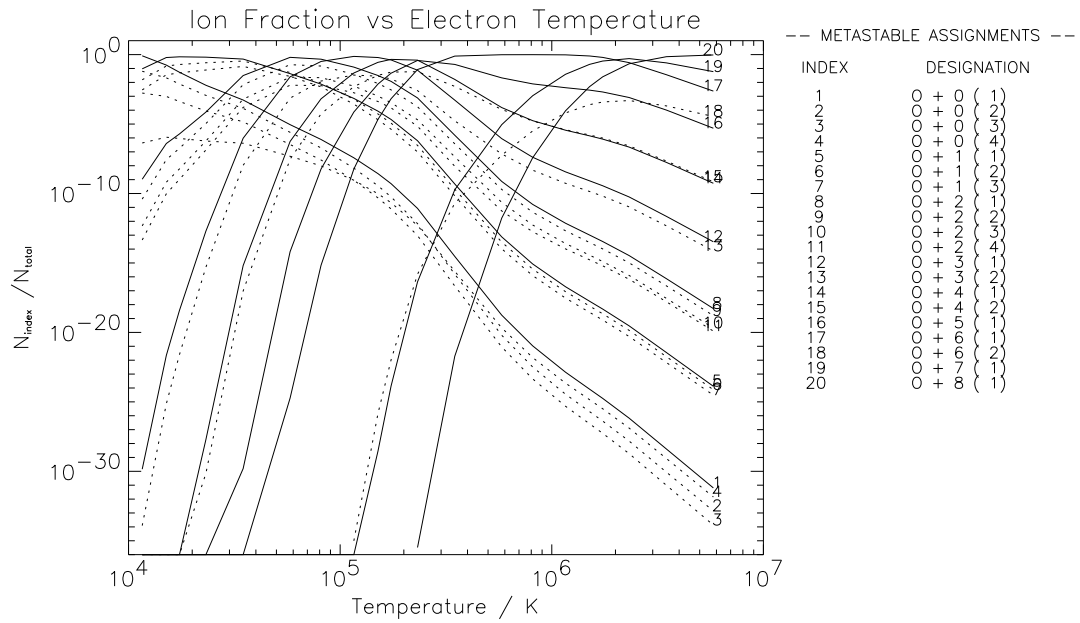


Figure 4.3: Metastable resolved equilibrium ionisation balance for oxygen. $N_e = 1.0 \times 10^{10} \text{ cm}^{-3}$. Metastable index designations on the right hand side correspond to the partition of table.4.12. Solid line - ground state, dotted lines - metastable states.

where $N_{tot} = \sum_{z=0}^8 N^z = \text{const.}$ in the usual metastable unresolved picture. Similarly, in the resolved picture, the ionisation fractional abundances are $\left. \frac{N^z}{N_{tot}} \right|_{\text{equil}}$ where $\sigma = 1, \dots, m_z$ and are as illustrated in fig.4.3.

The instantaneous effective radiated power coefficient associated with metastable σ of ionisation stage z , is P_σ^z . It is commonly separated as $P_{\sigma,LT}^z + P_{\sigma,RB}^z$ which distinguishes the parts of the power driven by excitation followed by line emission and the part driven by recombination. Bremsstrahlung is usually incorporated with the latter. The equilibrium radiated power function, P_{tot} , obtained by combining

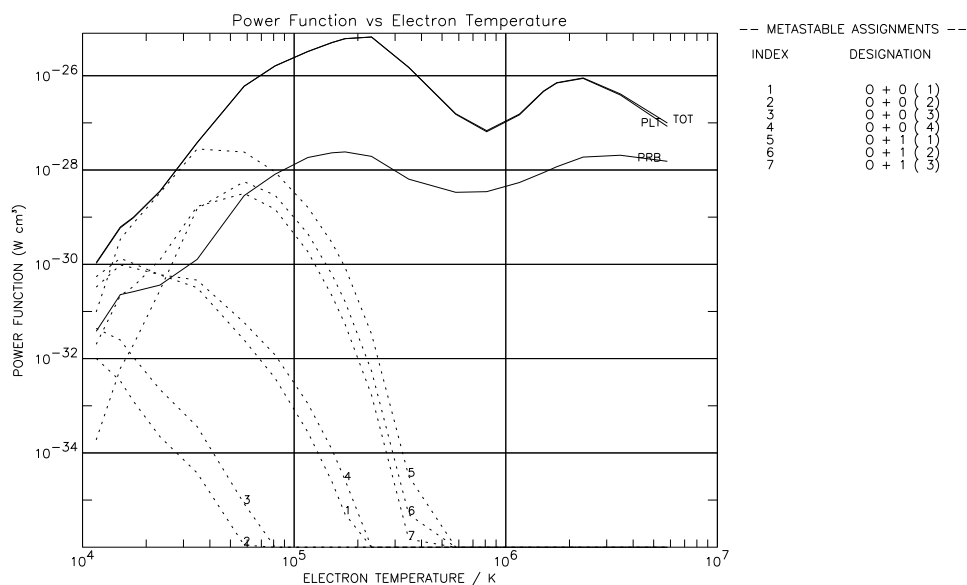


Figure 4.4: Contributions to the radiated power function of oxygen from low ionisation stage metastables i.e. O^{+0} and O^{+1} . $N_e = 1.0 \times 10^{10} \text{ cm}^{-3}$. Solid upper line - total, solid middle line - line power, solid lower line - Bremsstrahlung power, dotted lines - metastable contributions.

these coefficients with the equilibrium ionisation balance is,

$$P_{tot} = \sum_{z=0}^8 \sum_{\sigma=1}^{m_z} \left[P_{\sigma}^z \frac{N_{\sigma}^z(t \rightarrow \infty)}{N_{tot}} \Big|_{equil} \right] \quad (4.2)$$

The contribution in square brackets for the low ionisation stage metastables of oxygen is illustrated in fig.4.4.

An important quantity in fusion plasma studies, which plays a role also in the solar atmosphere, is the excess or deficit of radiated energy compared with that which would have been radiated in equilibrium. For example, the radiated energy from an inflowing O^{+0} atom, released from a limiter and entering a local high temperature plasma, which experiences a time dependent ionisation from its initial neutral state until equilibrium. For fixed electron density and temperature, the energy excess function is,

$$W_{excess} = \int_{t=0}^{\infty} \sum_{z=0}^{z_0} \sum_{\sigma=1}^{m_z} P_{\sigma}^z \frac{N^z(t) - N^z(t = \infty)}{N_{tot}} \quad (4.3)$$

with simpler equivalent quantities in the metastable unresolved picture.

4.3.2 Oxygen Excited Populations

Consider the O^{+3} ion. The adjacent ionisation stages are O^{+4} and O^{+2} . The levels of the O^{+3} ion can be separated into *metastable levels* O_{σ}^{+3} , where the Greek index σ spans the number of metastables, m_z , corresponding to two in this case i.e. $2s^22p^2P$ and $2s2p^2^4P$. Let the excited levels be denoted by O_{nl}^{+3} , where $nl = 1, \dots, \infty$ and n and l are themselves the usual principal quantum number and orbital angular momentum quantum number respectively. The driving mechanisms considered for populating the excited levels are, excitation from the metastable levels O_{σ}^{+3} , recombination from the metastable levels of the adjacent ion O_{τ}^{+4} and ionisation from the metastable levels of the adjacent ion O_{ρ}^{+2} , where ρ and τ index the metastable levels of these ions as given in table 4.12. The dominant population densities of the ions in the plasma are those of the levels O_{σ}^{+3} , O_{τ}^{+4} and O_{ρ}^{+2} , denoted by N_{σ} , N_{τ}^{+} and N_{ρ}^{-} respectively. The ratios of these dominant populations to $N(2s^22p^2P)$, the ground level, are assumed known from a separate calculation of a dynamical ionisation balance. The other populations

of significance in the plasma are the electron density N_e , the proton density N_p and the neutral hydrogen density N_H . A *quasi-static equilibrium* of the excited populations, with respect to these dominant populations, gives the connection between them as discussed in sec.2.2.2. Evaluation of the excited populations locally in the plasma, for this specific ion, is computed from the following equation,

$$N_{nl} = f_{nl,2s^2 2p \ 2P}^{(exc)} N_e N_{2s^2 2p \ 2P} + f_{nl,2s^2 p^2 \ 4P}^{(exc)} N_e N_{2s^2 p^2 \ 4P} \\ + f_{nl,2s^2 \ 1S}^{(rec)} N_e N_{2s^2 \ 1S} + f_{nl,2s^2 p \ 3P}^{(rec)} N_e N_{2s^2 p \ 3P} \quad (4.4)$$

where, for simplicity, terms arising from ionisation and charge exchange recombination have been omitted. The $f_{nl,\sigma}^{(exc)}$ and $f_{nl,\tau}^{(rec)}$ are the effective contributions to the excited populations from excitation from the metastables and from free electron capture by parent metastables respectively. The coefficients depend on density as well as temperature. This allows specification of the *excitation* photon emissivity coefficient,

$$\mathcal{PEC}_{2s^2 2p \ 2P, nl \rightarrow n'l'}^{(exc)} = (A_{nl \rightarrow n'l'} f_{nl,2s^2 2p \ 2P}^{(exc)}) / N_e \quad (4.5)$$

and the *recombination* photon emissivity coefficient

$$\mathcal{PEC}_{2s^2 \ 1S, nl \rightarrow n'l'}^{(rec)} = A_{nl \rightarrow n'l'} f_{nl,2s^2 \ 1S}^{(rec)} \quad (4.6)$$

and similar coefficients for the other metastables. That is each of these coefficients is associated with a particular metastable σ or τ of the O^{+3} or O^{+4} ions respectively. By combining these emissivity coefficients with the equilibrium ionisation balance metastable fractional abundances the *contribution functions*, $G_{nl \rightarrow n'l'}(T_e, N_e)$, are obtained. Specifications of these contribution functions differ slightly between solar astrophysical plasma and laboratory plasma usages. For astrophysical applications we define the contribution function to include the relationship between electron and hydrogen (ion+neutral) densities in the solar atmosphere. Thus, for our specific example,

$$G_{nl \rightarrow n'l'} = \frac{N_e}{N_H} \left[\mathcal{PEC}_{2s^2 2p \ 2P, nl \rightarrow n'l'}^{(exc)} \frac{N_{2s^2 2p \ 2P}^{+3}}{N_{tot}} \right]_{equil}$$

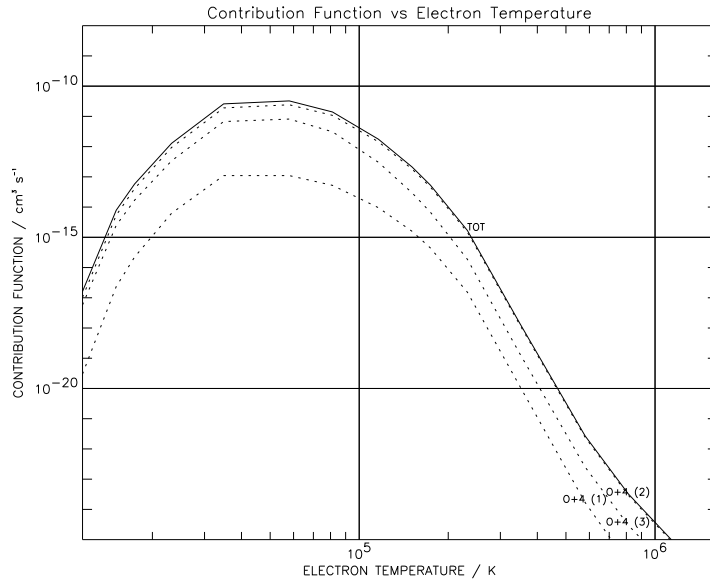


Figure 4.5: Contribution function for the $OII(2p^3 \ ^2D - 2s2p^4 \ ^4P)\lambda 718.5\text{\AA}$ transition showing the parts arising from the different metastables.

$$\begin{aligned}
 & +\mathcal{P}\mathcal{E}\mathcal{C}_{2s2p^2 \ ^4P, nl \rightarrow n'l'}^{(exc)} \frac{N_{2s2p^2 \ ^4P}^{+3}}{N_{tot}} \Bigg|_{equil} \\
 & +\mathcal{P}\mathcal{E}\mathcal{C}_{2s^2 \ ^1S, nl \rightarrow n'l'}^{(rec)} \frac{N_{2s^2 \ ^1S, nl \rightarrow n'l'}^{+4}}{N_{tot}} \Bigg|_{equil} \\
 & +\mathcal{P}\mathcal{E}\mathcal{C}_{2s2p \ ^3P, nl \rightarrow n'l'}^{(rec)} \frac{N_{2s2p \ ^3P, nl \rightarrow n'l'}^{+4}}{N_{tot}} \Bigg|_{equil} \quad (4.7)
 \end{aligned}$$

An illustration showing the localisation of the contribution function in temperature and the varying influence of metastable levels is given in fig.4.5.

4.4 Derived Recombination/Ionisation Rate Coefficients and the Resultant Ionisation Balance

In this work we use new calculations of dielectronic recombination in preparation of the generalised collisional dielectronic recombination coefficients. These data are incorporated from large structured datafiles in two ways. Firstly, direct state selective capture to identified low levels are extracted, combined with state selective radiative recombination data and added as an extension to the complete collisional rate coefficient/A-value/energy level data collection for these low levels. This is called a *specific ion file* which we have also referred to by its ADAS data format number, adf04. Secondly, dielectronic data grouped according to parent metastable and recombined ion principal quantum shell/spin system are drawn by a very many (bundle-nS) quantum shell collisional radiative calculation (see Burgess & Summers(1976)). Then in a final step, the bundle-nS results are projected onto the specific ion file low level data and the low level population calculation is completed. This yields also the metastable final ion/metastable initial parent ion collisional dielectronic coefficients (see chap.2, sec.2.2.2). The key issue is the accuracy and behaviour of these coefficients. Fig.4.6 shows the behaviour of the collisional-dielectronic coefficients with density. Capture from the beryllium-like (O^{+4}) $2s^2\ ^1S$ and $2s2p\ ^3P$ metastables is contrasted. Note the relatively small coefficient for the $2s2p\ ^3P$ metastable, due to the Auger break-up to the $2s^2\ ^1S$ parent. This coefficient is insensitive to the density until it gets very high, due to the secondary Auger process already depleting the excited states which for a non-metastable parent would be vulnerable to collisional re-ionisation. The collisional-dielectronic coefficient for capture from the $2s^2\ ^1S$ parent shows the usual density induced reduction at quite moderate densities and high temperatures. Note the increase with density of the coefficient at low temperatures in the radiative/three-body regime. Although for the densities of the solar chromosphere/transition region, the finite density results are required, most previous workers have used the total dielectronic recombination coefficient and thus limit their results to the case of zero density (e.g. Hahn(1985)). On some occasions an imprecise density dependent reduction is applied to the total zero-density coefficient, but this takes no true account

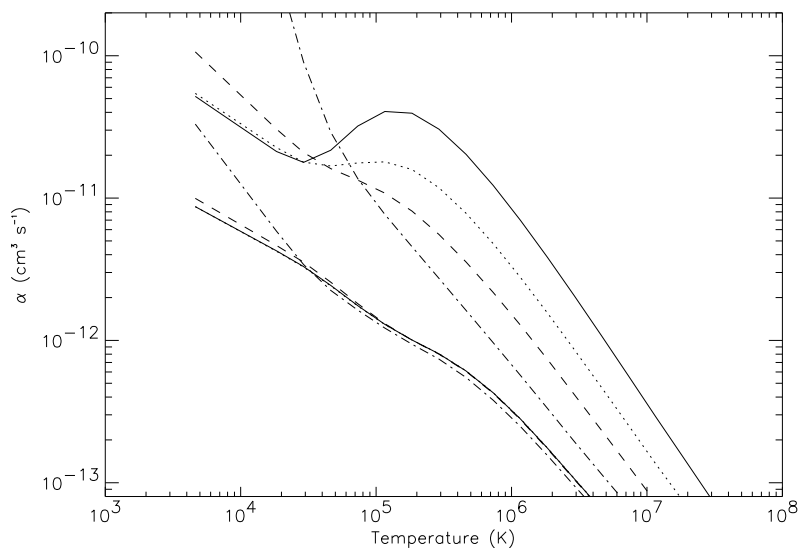


Figure 4.6: Generalised collisional dielectronic recombination coefficient example for $O^{+4}(2s^2\ ^1S \rightarrow 2s^2 2p\ ^2P)$ (upper solid line) and $O^{+4}(2s 2p\ ^3P \rightarrow 2s^2 2p\ ^2P)$ (lower solid line) as a function of temperature, for densities $N_e = 10^4$ - solid line, 10^{10} - dotted line, 10^{13} - dashed line and 10^{16} cm^{-3} - dash dot line.

of the distribution of recombination into excited states of the particular ion.

There is a problem at very low temperatures, $< 1.0 \times 10^4 \text{ K}$, when very few low autoionising levels contribute to the dielectronic coefficient and their precise energies are critical. The present calculations are based on LS-coupling and theoretical energy level calculations and so are inaccurate in this regime. At the temperatures of the transition region, the high temperature dielectronic recombination is more relevant. Corrections can be introduced to take account of low temperature dielectronic recombination (Storey et al.(1990)) but are not relevant here.

For the metastable resolved picture, resolution of ionisation rate coefficients by initial and final states is also required. Such data have not been available generally in the past. Ionisation cross-sections and rate coefficients are sometimes presented according to initial metastable but invariably summed over final states. In the work presented here, we have compensated for this deficiency by imposing a ‘resolution’ of

the total coefficient using the principles discussed by Burgess et al.(1977) and Summers & Hooper (1983). In a new development, we have commenced more detailed calculations of resolved ionisation rate coefficients and have established an organisation of the direct state resolved ionisation coefficients analogous to that used for state selective dielectronic and radiative recombination coefficients. These data may then be mapped into the low level specific ion files in like manner and then used in production of the generalised collisional dielectronic ionisation coefficients.

For $O^{+0} \rightarrow O^{+1}$, the rate coefficients involving ionisation from the 2p subshell were determined using the experimental data of Brook et al. (1978), for $O^{+1} \rightarrow O^{+2}$, that of Aitken et al.(1971) and for $O^{+2} \rightarrow O^{+3}$, that of Gregory et al.(1985). Details of the theoretical calculations and approximations used are given in Griffin(1995). In the general case, a substantial part of the task relates to excitation/autoionisation pathways (complementary to the dielectronic recombination situation). For the ions of oxygen, this appears less important. The extensions mentioned above have not yet been fully implemented in the central ADAS codes. They are scheduled for inclusion in mid 1997 together with a new very low temperature enhancement.

Of primary importance for solar astrophysics is the result of combining the recombination and ionisation data to form an equilibrium ionisation balance. As pointed out in sec.4.3.1, our primary ionisation balance is a metastable-resolved one. For assessment of the significance of the present developments and future comparison with earlier work we have used the equilibrium metastable to ground fractions, for each ionisation stage in the resolved picture, to reassemble a stage to stage ionisation balance.

It is to be noted that the ionisation balance is density dependent at moderate densities due to the dielectronic part, and at relatively high densities due to the stepwise ionisation part. Fig.4.7 contrasts the zero density balance with the balance at electron density $N_e \sim 5.0 \times 10^9 \text{ cm}^{-3}$, representing the upper solar transition region. The shifts of the stage abundance peaks compared with the zero density cases are given in table 4.13. The final definitive position on the ionisation balance and comparison to previous workers (e.g. Arnaud & Rothenflug (1985)) will not be presented until the extension defined above is completed. However, no substantive error is indicated

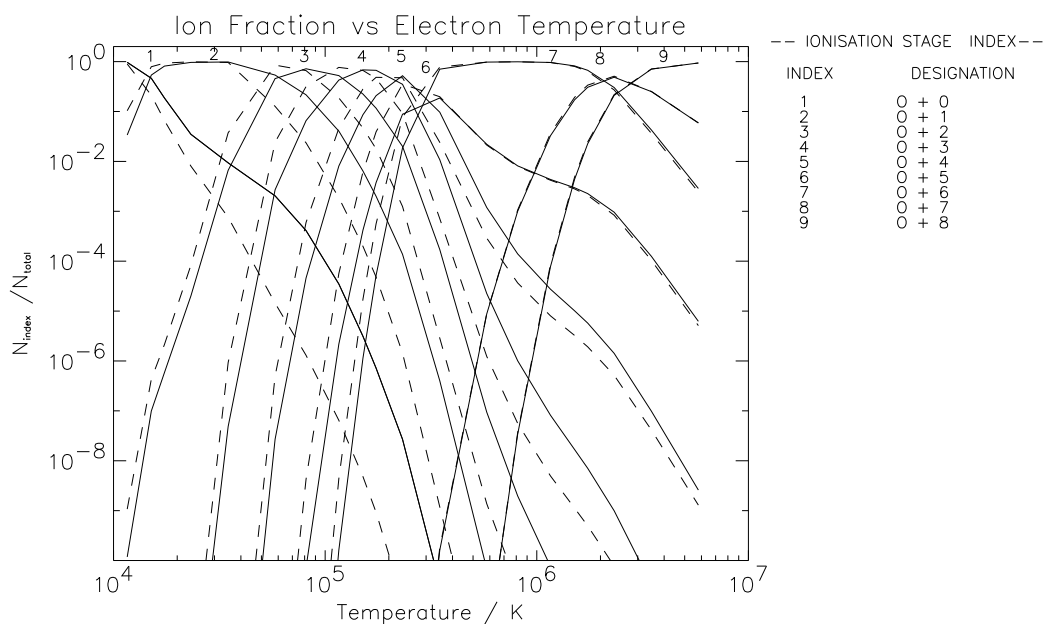


Figure 4.7: Comparison of reconstructed stage to stage ionisation balance at electron densities $N_e = 0.0$ (solid line) and $5.0 \times 10^9 \text{ cm}^{-3}$ (dashed line).

Ion	Temperature Displacement (K)	Ion	Temperature Displacement (K)
O^{+0}	s	O^{+5}	6.6×10^4
O^{+1}	3.0×10^3	O^{+6}	s
O^{+2}	2.1×10^4	O^{+7}	s
O^{+3}	4.7×10^4	O^{+8}	s
O^{+4}	2.7×10^4		

Table 4.13: Temperature displacement of the ionisation balance fractional abundance peaks as a result of density. An 's' denotes that the shifts were smaller than the temperature grid separations or that the peaks were so broad that the shifts were too small to notice (see fig.4.7).

in the present work.

4.5 Derived Populations and Emissivities

Turning to the spectroscopy of oxygen ions, we consider the influence of various factors on the populations of the excited states and then the emissivities. The individual electron impact excitation and deexcitation rate coefficients are of course fundamental in determining the final accuracy of any calculated emissivity. We have already explored the absolute precision of these cross-sections in sec.4.1.1. Here we examine rather the importance of finite plasma electron density, including or ignoring metastables and the coupling of low levels to the infinite higher n-shell populations for step-wise ionisation. Such examination is possible within our resolved picture. Fig.4.8 shows the emissivity coefficient for the transition $O^{+5}(5s\ ^2S - 2p\ ^2P)\lambda 117.4\text{\AA}$ as a function of electron density. This line illustrates the case of no metastables. Note that at an electron density $N_e = 1.0 \times 10^{14}\text{cm}^{-3}$, the $2p\ ^2P$ is already 10% of the ground population. Note the moderate decrease at higher electron densities and the increase due to the inclusion of step-wise ionisation pathways.

For emissivity coefficients of lines from an ionisation stage with metastables, the separate effective emissivities associated with each metastable are relevant. Effective coefficients are also present, associated with recombination and inner shell ionisation driven by the metastables of the adjacent stages. As in the ionisation balance case, we can reconstruct an unresolved emissivity coefficient by using the equilibrium metastable to ground fractions for each ionisation stage. Fig.4.9 illustrates these effects for $O^{+4}(2s3d\ ^3D - 2s2p\ ^3P)\lambda 192.9\text{\AA}$. Note that the excitation energies from the ground and metastable states to the $2s3d\ ^3D$ state are similar. Therefore, the spin changing contribution is smaller and the $2s2p\ ^3P$ metastable is more efficient at exciting the $2s3d\ ^3D$ state. Note also that the equilibrium reconstructed coefficient contains excitation contributions from both metastables. Exploration of other effects, for example the inclusion of excited state ionisation and recombination contributions to the line emission will be presented by Brooks et al.(1997).

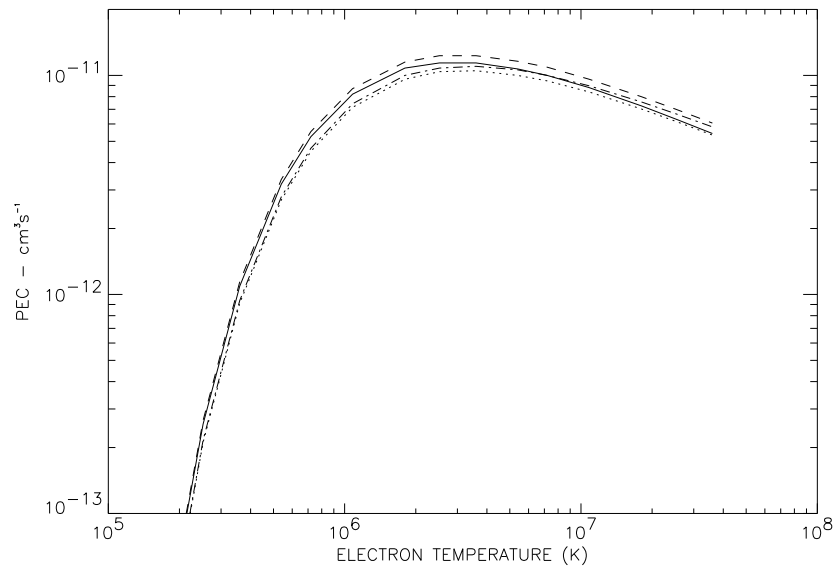


Figure 4.8: Influences on the $O^{+5}(5s\ ^2S - 2p\ ^2P)\lambda 117.4\text{\AA}$ line emissivity coefficient. Solid line - llu - low level metastable unresolved at $N_e = 10^{11}\text{cm}^{-3}$. Dotted line - llu at $N_e = 5 \times 10^{14}\text{cm}^{-3}$. dashed line - pju - high level pathways to ionisation and redistribution included, at $N_e = 10^{11}\text{cm}^{-3}$. Dash dot - pju at $N_e = 5 \times 10^{14}\text{cm}^{-3}$.

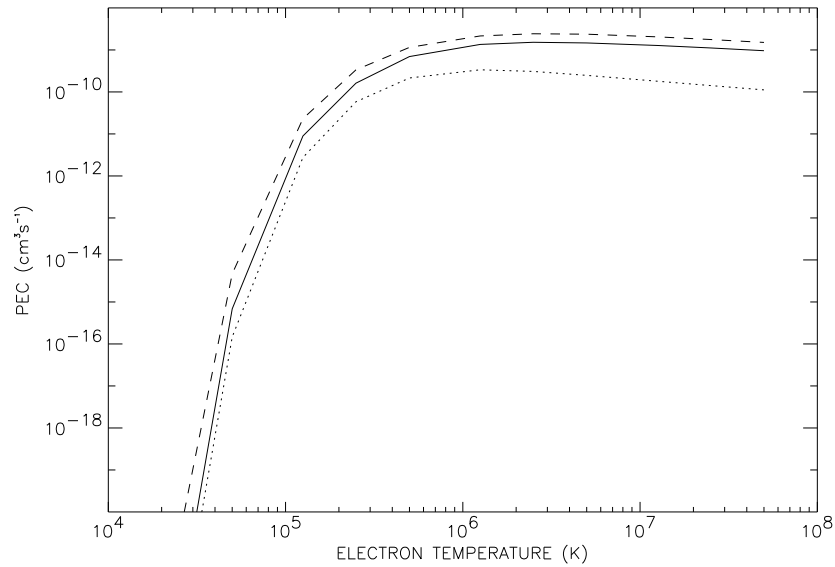


Figure 4.9: Effective emissivity coefficients for the $O^{+4}(2s3d\ ^3D - 2s2p\ ^3P)\lambda 192.9\text{\AA}$ line, from the $O^{+4}(2s^2\ ^1S)$ and $O^{+4}(2s2p\ ^3P)$ metastables. The results are presented at an electron density of $7.81 \times 10^{10}\text{cm}^{-3}$. The contribution from the $2s2p\ ^3P$ metastable is the dashed curve. The contribution from the $2s^2\ ^1S$ ground state is the dotted curve. The reconstructed stage emissivity for the excitation part is the solid curve.

4.6 Applications to Solar Atmospheric Structure

The important lines of oxygen ions for SOHO-CDS & SOHO-SUMER have been identified from our general script (see sec.4.2) with the aid of the review of sec.4.2). Data collections of $G(T_e)$ functions and spectrum line intensities of these lines are under preparation for solar atmospheric models, that is, linked pairs of electron density and electron temperature associated with height in the atmosphere. This is possible for, say, the various atmospheric models of Vernazza et al.(1981). For more general convenience, $G(T_e)$ functions for many transitions have been calculated and are stored in the central ADAS database for specific constant densities and constant pressures. The location of the $G(T_e)$ functions with temperature indicates the importance of particular spectrum lines for different parts of the atmospheres. Such considerations are of paramount importance if a differential emission measure analysis is to be attempted.

The effect of finite plasma electron density is again of paramount importance. For advancement of solar atmospheric studies to differential emission measures in density as well as temperature, it is of interest to know also the location of the $G(T_e, N_e)$ functions in density. This again can be linked to particular model heights in the atmosphere. More importantly, calculation of contribution functions dependent on density is essential for bi-variate DEM studies unless advantageous lines with weak density dependences have already been chosen. This however is a dangerous pastime as, anticipating the discussion of chap.5 sec.5.6.5, density dependences can be found in lines where it is not altogether expected. Fig. 4.10 shows the locations of the contribution functions for the OII($\lambda 833.8\text{\AA}$) and OV($\lambda 760.36\text{\AA}$) lines. The shifted positions in temperature are familiar and correspond roughly to upper chromosphere/lower transition region and upper transition region temperatures for OII and OV respectively. Note that the density dependence increases the line emission for OV and shifts it to lower temperatures before decreasing again at $1 \times 10^{15} \text{cm}^{-3}$. In the case of OII, the density dependence acts to decrease the line emission and shift it to lower temperatures while ‘peaking’ the function and decreasing the range of emission. The reduction is continuous for increasing density.

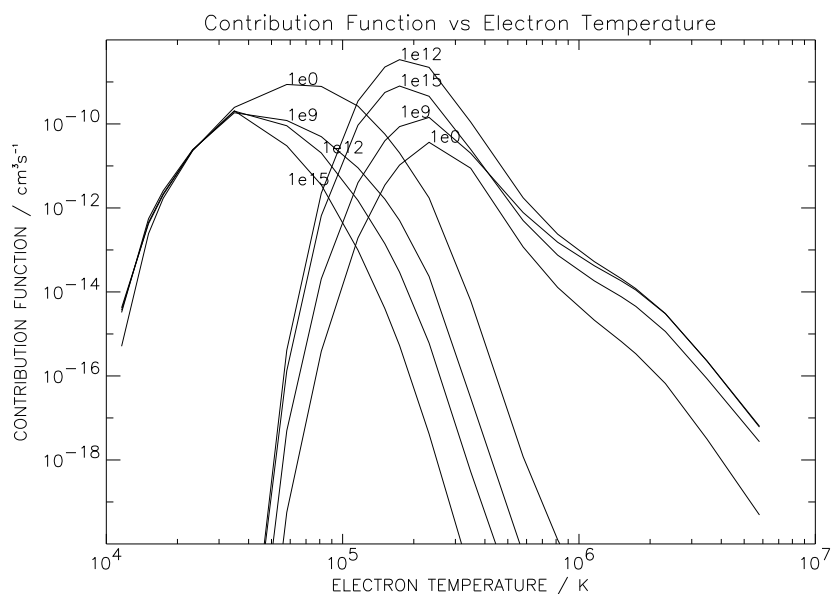


Figure 4.10: Contribution function for the $OV(2s2p\ ^3P - 2p^2\ ^3P)\lambda 760.36\text{\AA}$ and $OII(2p^3\ ^4S - 2s2p^4\ ^2D)\lambda 833.8\text{\AA}$ lines and the effect of finite plasma electron density.

4.7 Concluding Remarks

An extensive review of the fundamental electron impact excitation data for oxygen has been undertaken and the recommended data integrated into the ADAS database. These data have been combined with generalised collisional dielectronic recombination and ionisation data to calculate a metastable resolved equilibrium ionisation balance for oxygen using the numerical technique outlined in chap.3 sec.3.2.1. This allowed detailed examination of the role of metastable states in the ionisation balance and spectral emissivities.

We have shown that non-ground state metastables can contribute substantially to contribution functions, equilibrium photon emissivities and radiated power. In addition, they can attain populations comparable to ground states. Previous work in the fusion context has also shown that metastable states can shift the reconstructed ionisation stage peaks in temperature due to their effects on ionisation coefficients

(Dickson (1993)). From chap.2 sec.2.1.2 we see that metastable states have lifetimes comparable with timescales for plasma transport. As pointed out in sec.4.3.1 the metastable resolved picture is mandatory here. To model radiated power and spectral intensities in such environments also requires a metastable resolved transient ionisation model. ADAS provides a capability to calculate a transient ionisation balance for a system evolving from a dynamic state until equilibrium and computes associated radiated energy and emission excesses/deficits. Investigation of these effects is part of our paper study.

By inclusion of the dielectronic data we allowed investigation of the associated effects of finite plasma density on the ionisation balance, contribution functions etc. It is clear that even at moderate alterations from zero density the ionisation balance and contribution function peaks shift and the shapes can change substantially. Incorporation of density dependencies to spectral emission prediction is essential for furthering solar analysis by development of commonly used methods such as differential emission measure. We will return to this topic in the discussion section of the next chapter.